ACS APPLIED MATERIALS & INTERFACES
Research Article
www.acsami.org

Optimization of Aerosol Jet Printing for High-Resolution, High-Aspect Ratio Silver Lines

Ankit Mahajan, C. Daniel Frisbie,* and Lorraine F. Francis*

Department of Chemical Engineering and Materials Science, University of Minnesota, Minneapolis, Minnesota 55455, United States

Supporting Information

ABSTRACT: Aerosol jet printing requires control of a number of process parameters, including the flow rate of the carrier gas that transports the aerosol mist to the substrate, the flow rate of the sheath gas that collimates the aerosol into a narrow beam, and the speed of the stage that transports the substrate beneath the beam. In this paper, the influence of process parameters on the geometry of aerosol-jet-printed silver lines is studied with the aim of creating high-resolution conductive lines of high current carrying capacity. A systematic study of process conditions revealed a key parameter: the ratio of the sheath gas flow rate to the carrier gas flow rate, defined here as the focusing ratio. Line width decreases with increasing the focusing ratio and stage speed. Simultaneously, the thickness increases with increasing the focusing ratio but decreases with increasing stage speed. Geometry control also influences the resistance per unit length and single pass printing of low-resistance silver lines is demonstrated. The results are used to develop an operability window and locate the regime for printing tall and narrow silver lines in a single pass. Under optimum conditions, lines as narrow as 20 μm with aspect ratios (thickness/width) greater than 0.1 are obtained.

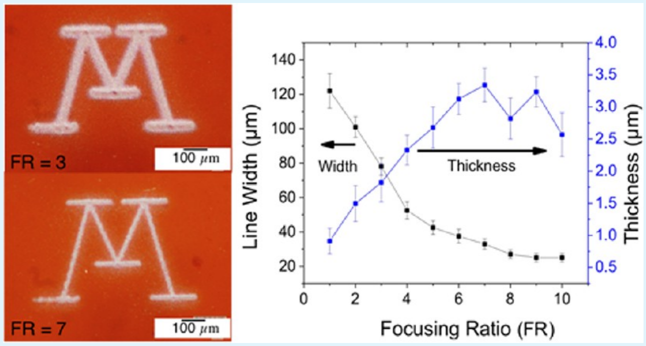

KEYWORDS: *aerosol jet printing, printed electronics, focusing ratio, printed silver lines, high resolution, operability window*

1. INTRODUCTION

In recent years, printing processes have gained interest as means to fabricate low-cost, large-area electronic circuits and devices on flexible, plastic substrates.[1] A variety of methods, including screen printing, inkjet printing, flexography, gravure printing, and aerosol jet printing, have potential.[2−5] However, there are many demands on these processes. Electronic devices, such as organic light-emitting diodes and thin film transistors, are multilayered and require excellent control over the feature size and placement. Resolution, or the minimum feature size, is also central to creating high-density circuits. Further, devices are built from a variety of materials and therefore, printing processes should allow for printing of inks with a range of properties. Lastly, for most efficient production, printing processes should be capable of integration into a roll-to-roll manufacturing line. The effects of process parameters, such as deposition speed, on the quality of the printed circuit elements must be understood for candidate printing processes. In this paper, we focus on the effect of printing process parameters on the aerosol jet printing of conductive networks.

Conductive lines require both narrow width for high-density circuitry, and sufficient thickness for large cross-sectional area and high current carrying capacity. Therefore, a goal for printing conductive networks is to create lines with high resolution (low line width) and high aspect ratio, where aspect ratio is defined as the ratio of thickness to the width of the lines. These constraints are frequently difficult to achieve simultaneously at high printing speeds. In aerosol jet printing, thicker lines have been achieved by multiple passes.[6−8] However, this strategy is inefficient and leads to an increase in the width of the printed lines.

Aerosol jet printing is a relatively new method for fabrication of printed electronics. In this method,[9] the functional ink is aerosolized and entrained in a gas stream. There are two options for generating the aerosol: pneumatic and ultrasonic. The aerosol stream is directed to a print head where it is aerodynamically focused by a coaxial sheath gas flow, as shown in Figure 1. The result is a high-density deposit with feature size only a fraction of the nozzle opening. The technique is suitable for printing conductors, semiconductors, and dielectrics. As a consequence, there has been recent interest in using the method for a variety of applications, including printing of transistors,[10−14] strain gauges,[15] interconnects,[16] electrode arrays,[17] solid oxide fuel cells,[18,19] and solar cells.[6,20−24]

Although most of the past reports demonstrate the technique's applicability, there are very few studies examining the factors that affect the printing quality. Goth et al.[8] studied printing of silver lines with an aerosol jet printer outfitted with a pneumatic atomizer. They showed that the width of the printed lines is affected by the three adjustable flow rates on

Received: February 16, 2013
Accepted: May 9, 2013
Published: May 9, 2013

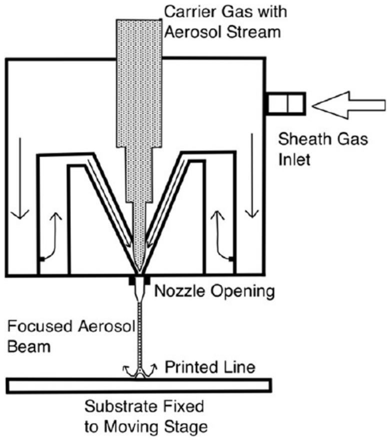

Figure 1. Schematic of the aerosol jet print head showing aerodynamic focusing by sheath gas inside the print head.

their instrument and the stage speed; however, regarding thickness control, they focused on the effect of number of layers deposited. Verheecke et al.[25] also studied printing with a pneumatic atomizer and developed a process window showing the effects of the three gas flow rates on the edge definition of the printed lines. Although these studies reveal some information on the printing process, they are specific to the pneumatic atomizer and cover only a portion of the process parameters. More research is needed on printing with the ultrasonic atomizer, which is well-suited to lower viscosity inks and arguably has tighter control of the aerosol mist particle size, and on the effects of full range of process variables on the characteristics of printed lines.

The aerosol jet printing process with the ultrasonic atomizer is influenced by a number of variables. The adjustable process parameters include the atomization frequency, carrier gas flow rate, sheath gas flow rate, nozzle diameter, working distance, stage speed, and stage temperature. Additionally, the surface tension, solids loading and viscosity of the ink play crucial roles in obtaining a wide range of structures from tall interconnects to thin capacitor films. In this work, we systematically study the influence of process parameters on geometry and electrical properties of lines created from silver nanoparticle ink. By exploring these process parameters in combination, we identify a key parameter, the focusing ratio, which is defined as

$$\text{focusing ratio (FR)} = \frac{\text{sheath gas flow rate}}{\text{carrier gas flow rate}} \qquad (1)$$

Although the role of the sheath gas in focusing the aerosol is recognized, we demonstrate here that the focusing ratio is central to controlling the line features and resistance. Additionally, the results are used to develop an operability window and process regime for printing tall and narrow silver lines in a single pass.

2. MATERIALS AND METHODS

All printing experiments were carried out with a nanoparticle silver ink (UTDAg40X, UT Dots Inc.). This ink is compatible with the ultrasonic atomizer of the aerosol jet printer, which has a recommended ink viscosity range of 1−5 cP. The ink contains 40% by weight of the silver nanoparticles (8−15 nm in diameter) in a solvent mixture of xylene and other hydrocarbons (proprietary). For each printing run, a glass vial was loaded with 1.70 mL of the ink and 0.30 mL (15% v/v) terpineol as a cosolvent. During atomization, the ink vial was maintained at a constant temperature (14 °C) using a temperature stabilized water bath.

Silver lines were printed in a single pass using a commercial Aerosol Jet Printer (M^3D, Optomec Inc.). Dry N_2 (HP grade, 99.998%) was used as the carrier and sheath gas. Experiments were carried out with carrier gas and sheath gas flow rates ranging from 0 to 50 standard cubic centimeters per minute (sccm) and 0−200 sccm, respectively. Three different nozzle sizes (100, 150, and 200 μm) were used; each nozzle is 7.50 mm long. The atomizer current was kept constant at 0.60 mA and the printer stage heater was not used. Stage speeds were varied from 1 to 100 mm/s. Printing was done both on polyimide (3 mils Kapton, DuPont) and silicon substrates. The ink showed good wetting on both substrates and hence no surface pretreatment was required. Unless otherwise noted, the results show data for printing on silicon. All printed lines were sintered in an oven at 200 °C for 1 h.

The geometrical features, microstructures, and electrical properties of the printed lines were characterized. Line widths were measured using the Alignment Viewer optical microscope that is incorporated into the printer. With this method, we could exclude any overspray and characterize the electrically functional part of the line. The line thicknesses were measured after sintering using a Tencor P-16 profilometer. Because of the parabolic cross-section of the lines, the total thickness was taken as the average thickness of the cross-section. An example profilometer trace is shown in Figure 2. The lines were also imaged using a Hirox microscope (Digital Microscope KH-7700) and a scanning electron microscope (JEOL-6500). To measure the electrical conductivity, we printed silver pads and lines, as shown in Figure 3a. The conductivity measurements were made using the two-point probe method in a N_2-filled glovebox with Keithley 236 electrometers.

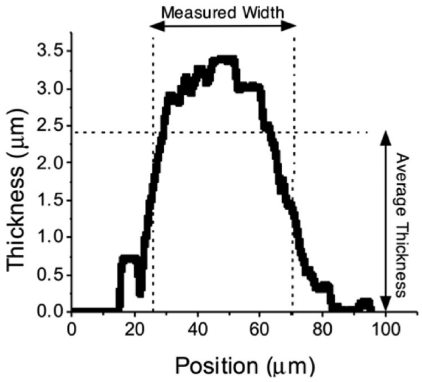

Figure 2. Cross-sectional profile of a printed silver line obtained from surface profilometry. This data provided the average thickness (2.41 μm). The width, measured in the optical microscope (45 μm), is also shown.

3. RESULTS

3.1. Effect of Processing Parameters.

Figure 3 shows the versatility of aerosol jet printing. Silver lines were printed on flexible polyimide substrates (Figure 3a), over surface topology (Figure 3b), and in complex and high-resolution patterns (Figure 3c, d). The quality and features of the printed patterns are determined by several printing processing parameters as well as the properties of the ink. An important process parameter is the focusing ratio (eq 1), as demonstrated in Figure 3e−g. In this paper, we explore the key adjustable printing parameters: focusing ratio, nozzle size, carrier gas flow rate, and stage speed. For simplicity, the same ink was used for printing and efforts were made to keep all other conditions the same. In particular, the distance between the nozzle tip and the substrate, i.e., the working distance, has some impact on

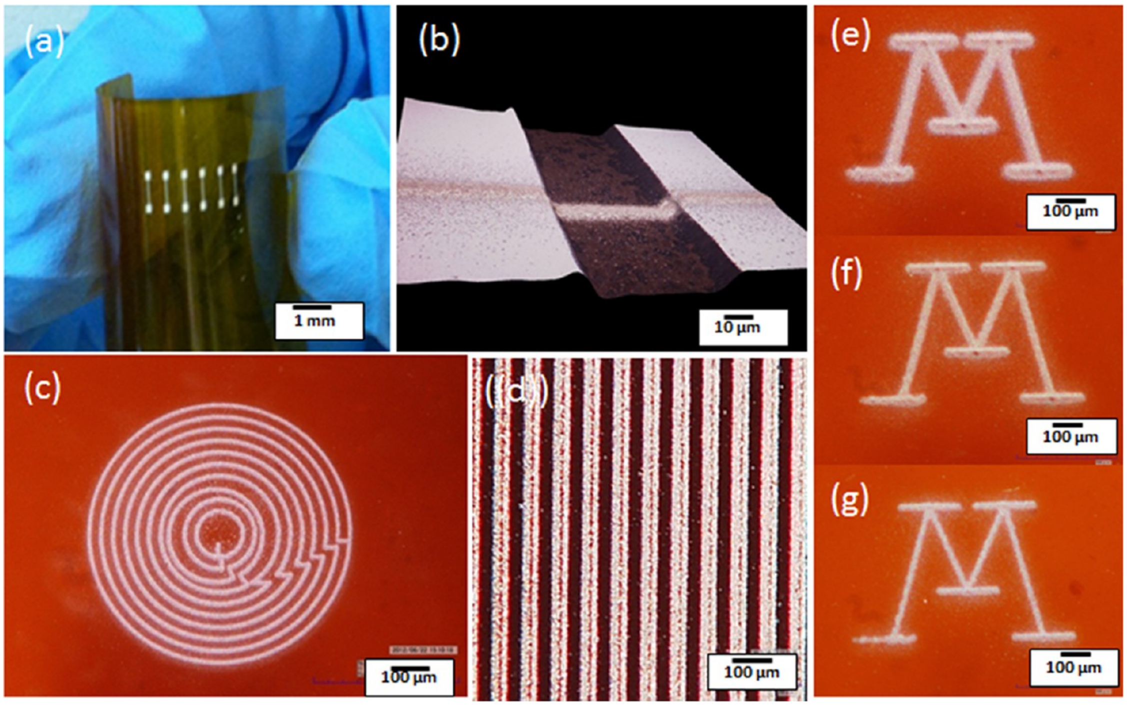

Figure 3. Images of different printed silver patterns: (a) printed pads and lines on flexible polyimide substrate for electrical characterization; (b) topographical image of a line printed over a 10 μm deep trench with slightly tapered walls etched in silicon; (c) printed spiral pattern on polyimide; (d) 40 μm wide lines with 30 μm spacing; and University of Minnesota logo printed at focusing ratio (e) 3, (f) 5, and (g) 7.

printing but was kept constant at 2 mm. This value produced a highly collimated aerosol beam for all focusing ratios investigated. See Figure S1 in the Supporting Information.

Figure 4a shows the effect of focusing ratio on the line width and thickness for a fixed nozzle diameter (200 μm), carrier gas flow rate (20 sccm) and stage speed (2 mm/s). The line width decreases as the focusing ratio increases up until a focusing ratio of about 8. Beyond this value, the width is nearly constant. Extremely wide lines, such as 120 μm, are obtained for a focusing ratio of 1 whereas lines as narrow as 25 μm are obtained for higher focusing ratios. The error bars represent the variability from run to run expressed as standard deviation. The variations in width become smaller as the focusing ratio increases. Unlike the width, the line thickness variations increase with the focusing ratio. The trend is also demonstrated in the profilometry scan results shown in Figure 4b. Overall, the thickness has more variability than the line width. As described more below, the thickness is affected significantly by the carrier gas flow rate and is subject to fluctuation based on the aerosol output. Above a FR of 8, the thickness becomes more erratic, not increasing as expected. This behavior may be due to change in the aerosol flow characteristics or premature drying brought about by the high sheath gas flow rate. These effects require more investigation, but in practice regions of high variability are avoided.

The line width and thickness are also a function of nozzle size. Figure 5 shows the effect of nozzle diameter and focusing at constant carrier gas flow rate (16 sccm) and stage speed (2 mm/s). As expected, finer lines are produced from smaller nozzles. Interestingly, the drop in line width with increasing focusing ratio is more dramatic in the smaller nozzles. However, there is a limitation; pressure builds up in the nozzle as focusing ratio increases. For smaller nozzles, the pressure limitation is reached at lower focusing ratios as compared with larger nozzles. See Figure S2 in the Supporting Information. Hence, the line width reaches a limiting value that is independent of the nozzle diameter. Except for the extremely wide lines, almost

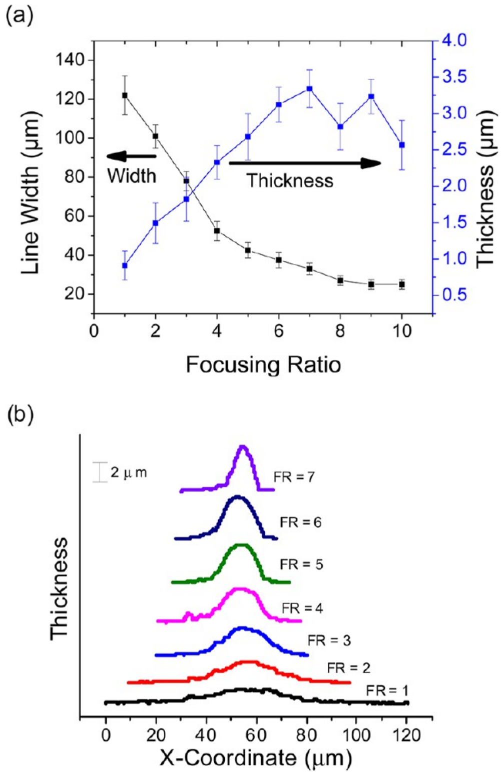

Figure 4. (a) Effect of focusing ratio on line width and thickness. (b) 2D profilometry data of lines printed for focusing ratios from 1 to 7. The carrier gas flow rate and stage speed are fixed at 20 sccm and 2 mm/s, respectively.

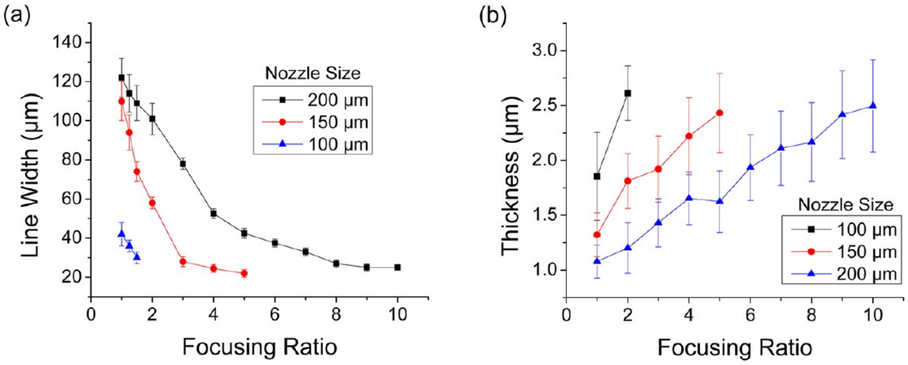

Figure 5. Effect of nozzle size on (a) line width and (b) thickness. The carrier gas flow rate and stage speed are kept constant at 16 sccm and 2 mm/s, respectively.

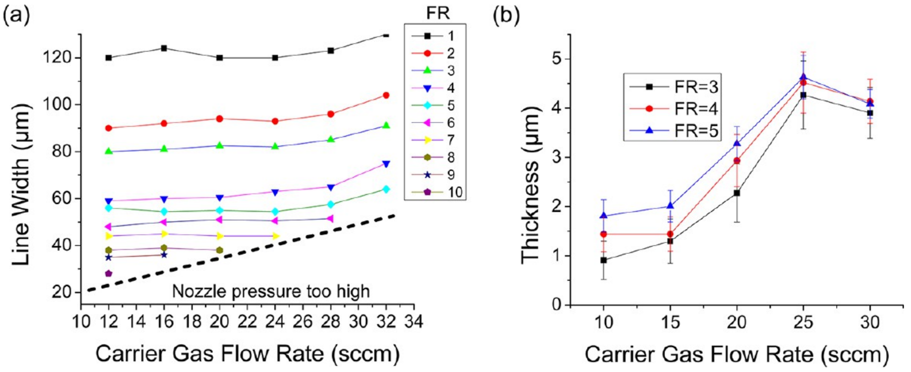

Figure 6. Effect of carrier gas flow rate on (a) line width and (b) thickness for different focusing ratios. The stage speed used is 2 mm/s.

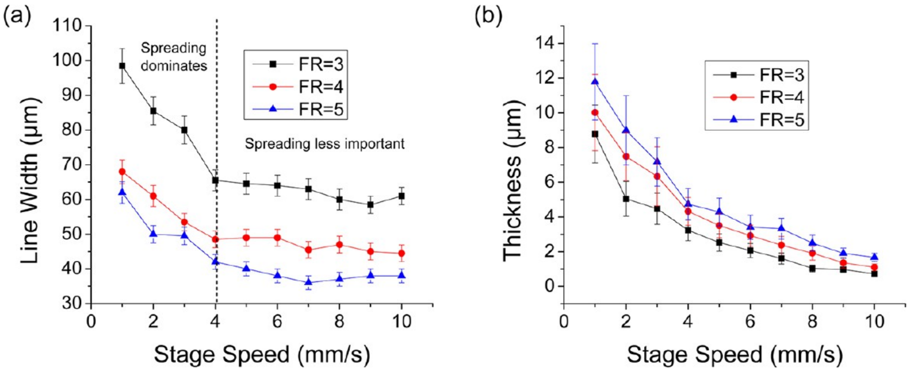

Figure 7. Effect of stage speed on (a) line width and (b) thickness for different focusing ratios. The carrier gas flow rate is fixed at 24 sccm.

the entire spectrum of line widths achieved using a 200 μm nozzle can be achieved with a 150 μm nozzle at comparatively lower sheath gas flow rates. Figure 5b shows the variation in thickness of the same lines with nozzle size and focusing ratio. For a given focusing ratio, the thickness increases with a decrease in the nozzle diameter. All the three nozzle diameters yield almost the same maximum thickness but the minimum thickness is lower in the 200 μm nozzle. It is evident that the 200 μm nozzle yields a wider range of both line width and thickness and sustains higher sheath gas flow rates. Consequently, the 200 μm nozzle was used for the rest of the work.

Panels a and b in Figure 6 show the effect of carrier gas flow rate on the line width and thickness, respectively, at different focusing ratios and constant stage speed of 2 mm/s. For most carrier gas flow rates, the line width depends on the ratio of sheath gas flow rate to carrier gas flow rate and not the respective values. This result laid the basis for the definition of focusing ratio, which is used extensively in this work. A slight deviation in the trend is found for carrier gas flow rates greater than 30 sccm. Here, the width begins to increase, consistent with spreading after deposition. Note that the nozzle pressure limitation restricts the carrier gas flow rates that can be used at high focusing ratios. Unlike the line width, the thickness changes considerably with the carrier gas flow rate. Thickness increases with carrier gas flow rates until at higher flow rates it falls off again because of spreading after deposition. As before, for the same carrier gas flow rate, the thickness is higher at higher focusing ratios.

Line geometry is further modified by stage speed, as demonstrated in Figure 7a. The data show how stage speed affects the line width at different focusing ratios for a given carrier gas flow rate. Line width decreases steadily as stage speed increases from 1 to 4 mm/s and then saturates. As discussed later, spreading influences this trend. Thickness decreases continuously with stage speed (Figure 7b). Similar trends are also observed for various focusing ratios. The effect of the major process variables on the line width and thickness are summarized in Table 1.

Table 1. Effect of Independently Increasing Each of the Process Variables on Printed Line Geometry

Process Variable	Line Width	Line Thickness
Focusing Ratio	Decreases	Increases
Nozzle Diameter	Increases	Decreases
Carrier Gas Flow Rate	Remains the Same	Increases
Stage Speed	Decreases	Decreases

3.2. Electrical Properties.

Figure 8 shows the effect of the process parameters on the electrical properties of the sintered silver lines. The resistance of lines is displayed on a per mm basis after subtracting the contact resistance. Details of contact resistance determination are in the Supporting Information section. The calculated resistivity is 3.61 $\mu\Omega$ cm, which translates to approximately twice that of bulk silver, on par with other reported values for printed silver lines.[26,27]

As shown in Figure 8a, the resistance per unit length is approximately independent of focusing ratio for a fixed carrier gas rate and stage speed. The exception is an increase in resistance that occurs at low focusing ratio and low carrier gas flow rate (14 sccm). Under these conditions, the lines were noticeably less dense than the lines printed under other conditions. Resistance per unit length also increases with the stage speed, as shown in Figure 8b. The dependence is linear up to a certain stage speed. Here, conductive lines are printed at stage speeds as high as 100 mm/s. This high speed printing requires a relatively large carrier gas flow rate to ensure adequate material for deposition. It was also observed that at stage speeds above 10 mm/s, printing began with a snakelike deposition as the stationary stage accelerated to a very high speed. The wiggle from this inertial effect straightens out once the stage attains a constant velocity.

4. DISCUSSION

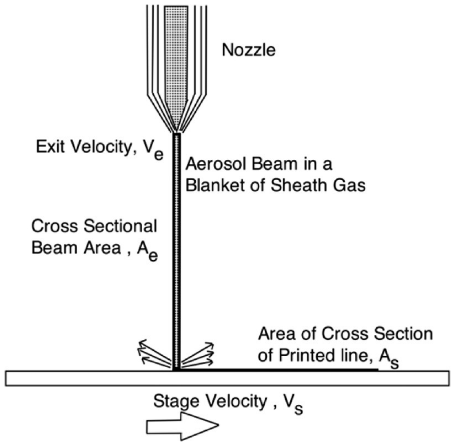

Figure 9. Enlarged view of the nozzle showing physical features as the aerosol jet exits the nozzle and meets the moving substrate to form a printed line. Upon impact, the aerosol beam coalesces and the gases are expelled.

4.1. Physical Principles of Aerosol Jet Printing.

Figure 9 is a schematic diagram showing the physical features of the aerosol beam from nozzle to substrate and the connection to the geometry of the as-printed line. The sheath gas forms an outer layer around the aerosol stream and prevents the contact between the aerosol particles with the inside walls of the nozzle, preventing clogging. The collimation of the aerosol beam takes place in two stages.[9] Prior to the nozzle (see Figure 1), the sheath gas surrounds the aerosol stream as it passes through a first orifice. Next, the combined sheath gas and aerosol stream is focused further as it passes through the narrower nozzle. The combined sheath and aerosol beam is accelerated to an exit velocity, V_e, creating an aerosol stream with cross-sectional area A_e.

If there is no loss of material, the mass flow rate at the point of exit from the nozzle and at the point where the aerosol beam hits the substrate are the same, and the continuity equation applies

$$\rho_e A_e V_e = \rho_s A_s V_s \tag{2}$$

where A_s and V_s are the cross sectional area of the printed line and stage speed, respectively, and ρ_e and ρ_s are the densities of the aerosol beam and the coalesced as-printed material, respectively. Rearranging, the factors that control the width, w, and thickness, t of the as-printed line are given by

$$wt \approx A_s = \left(\frac{\rho_e}{\rho_s}\right)\frac{V_e A_e}{V_s} \tag{3}$$

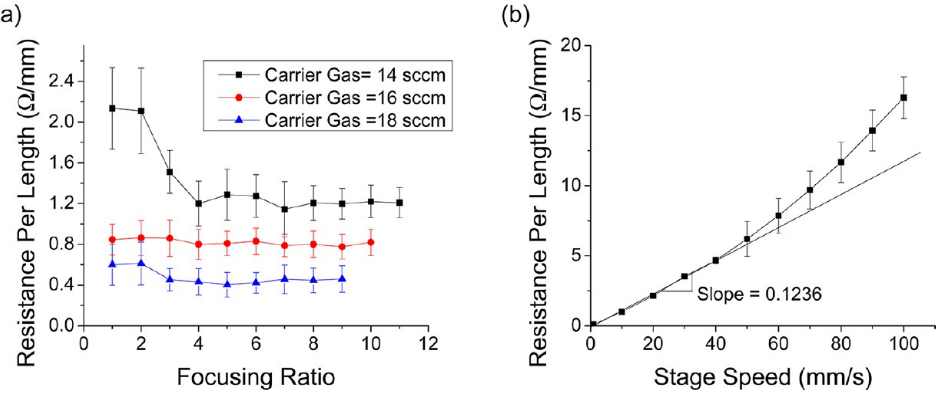

Figure 8. Electrical properties of printed lines. (a) Dependence of the resistance per unit length on the focusing ratio and the carrier gas flow rate (stage speed = 2 mm/s). (b) Effect of stage speed on resistance per unit length (carrier gas flow rate = 40 sccm and the FR = 3).

Upon impingement, the aerosol droplets coalesce to form a liquid line. The width of the printed line is the sum of the diameter of the collimated beam and lateral spreading after deposition. It should be noted that A_s is different from the final cross-sectional area because of the decrease in thickness from evaporation and sintering. Although this simple picture does not address the details of how the aerosol stream condenses into a printed line and the subsequent spreading, evaporation, and sintering, it does help to explain the observed effects of process parameters on the printed line geometry as summarized in Table 1.

4.2. Effect of Process Parameters on Line Geometry. For a fixed carrier gas flow rate and stage speed, the line width decreases and thickness increases with an increase in the sheath gas flow rate or in other words with an increase in the focusing ratio (Figure 4). Increasing the sheath gas flow rate tightens the aerosol beam and reduces the cross sectional area of the beam at the exit, A_e. Assuming ρ_e is constant, the reduction in A_e also leads to an increase in V_e such that the product, A_eV_e is a constant (by conservation of mass). Assuming that ρ_s does not change much for different sheath gas flow rates, it can be seen from eq 3 that the product of width and thickness is also a constant for a fixed stage speed. The width and the thickness of the as-printed line are therefore hyperbolically related to each other, as shown schematically in Figure 10. On each of the hyperbolas, increasing the focusing ratio leads to a decrease in the width and increase in the thickness but the cross-sectional area and hence the resistance per length of the printed line (see Figure 8a) remains the same, as described more below.

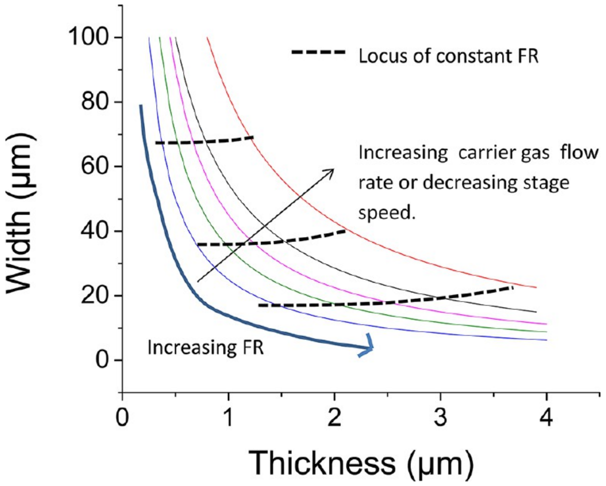

Figure 10. Schematic showing line width and thickness variation with focusing ratio for different carrier gas flow rates (at fixed stage speed) or different stage speeds (at fixed carrier gas flow rate) based on the conservation of mass equation. Numerical values on the axes are estimates for as-printed lines before drying and sintering.

Line width is found to be nearly the same for a fixed value of focusing ratio and stage speed irrespective of the carrier gas flow rate, as shown in Figure 6a. We believe that the coaxial carrier and sheath gas flow inside the nozzle readjusts to yield similar beam diameter as long as both the flow rates remain proportionate. In terms of eq 2, increasing the carrier gas flow rate at fixed focusing ratio results in an increase in the V_e while keeping A_e constant; hence, we expect A_s to increase. This increase can also be represented by a different hyperbola for each value of carrier gas flow rate, as shown in Figure 10. Because the beam diameter is fixed, the increase in A_s is accommodated by an increase in thickness. Therefore, moving to the right on the constant FR lines (Figure 6), there is no change in the line width but the thickness keeps increasing, also shown in Figure 6b.The effect of nozzle diameter can be likewise understood. See Figure S4 in the Supporting Information.

Increasing the stage speed at a fixed carrier and sheath gas flow rate further lowers the line width and thickness, as illustrated in panels a and b in Figure 7, respectively. This effect can be directly related to eq 3. Namely, increasing V_s with all else constant requires A_s to decrease. Therefore, each hyperbola in Figure 10 corresponds to a certain stage speed. Although the decrease in thickness with stage speed is expected, the variation of line width with stage speed is less expected. Line width varies greatly with stage speed at slower speeds and becomes more or less constant after a certain speed, as shown in Figure 7a. This general trend is represented qualitatively in Figure 10 where for a fixed focusing ratio, line width starts to increase below a specific stage speed. Spreading becomes an important factor in determining line widths when the ink accumulates on the substrate at a rate that the amount of solvent in the printed line after coalescence is appreciable. This phenomenon is more pronounced at low stage speeds (Figure 7a, stage speed <4 mm/s) and high carrier gas flow rates (Figure 6a, carrier gas >30 sccm). Under these conditions, a large amount of liquid accumulates over a fixed width determined by the focusing ratio. This constrained build-up leads to a nonequilibrium curvature of the liquid just after coalescence. Consequently, there is fluid flow driven by surface tension and curvature gradients, causing an increase in line width. Eventually, the liquid attains its equilibrium curvature dictated by the contact angle. At high stage speeds or low carrier gas flow rates, the curvature of the coalesced liquid is close to its equilibrium value and therefore spreading is not dominant. Almost no decrease in line width is observed at higher stage speeds (Figure 7a), suggesting the reduced importance of spreading and the sole dependence of the width on the beam diameter.

Focusing is crucial in aerosol jet printing; however, several factors limit the focusing ratio. One factor is the maximum pressure limit of the nozzle. As the flow rates for the sheath and carrier gas increase, the pressure exerted on the nozzle also increases, eventually reaching a limiting value. Additionally, at higher focusing ratios there is a possibility of departure from laminar flow behavior of the combined aerosol and sheath gas jet as indicated by the unexpected thickness variation after FR of 8 in Figure 4a. Focusing ratio, ultimately, is limited by the fact that the gases inside the nozzle cannot exceed the sonic velocity (the maximum velocity to which a fluid can be accelerated in a converging nozzle).

A phenomenological problem with aerosol jet printing is overspray (Figure 11). Overspray is harmful not only for the loss of material but also because it renders aerosol jet printing unfit for printing narrowly spaced lines such as a source-drain channel in transistors. Overspray is a complex phenomenon and is dominant at high sheath gas flow rates, slower stage speeds, and high working distances. The physical principles behind overspray are still not completely understood. Overspray can be quantified in two ways: density and spread. One possible strategy to study overspray could be to predefine allowable values of these parameters and use image analysis to measure overspray as process variables change. Studies are underway to study the effect of process variables on overspray.

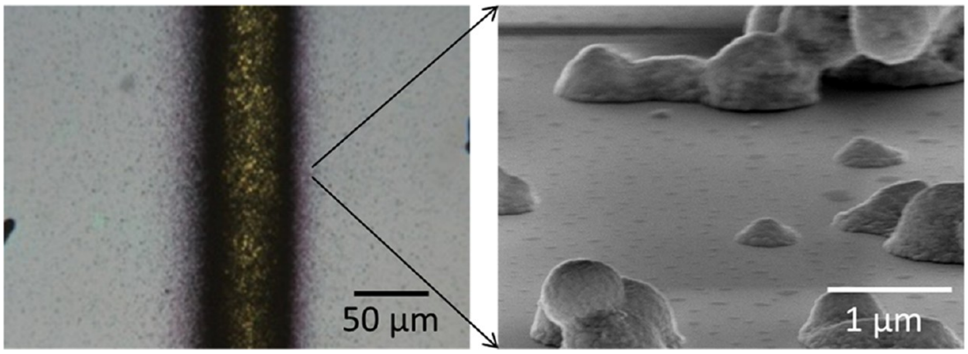

Figure 11. Phenomenon of overspray. (a) Optical microscope image of overspray on either side of a printed and sintered silver line on a silicon wafer. (b) SEM image of the same region showing overspray as tiny clusters of sintered silver nanoparticles.

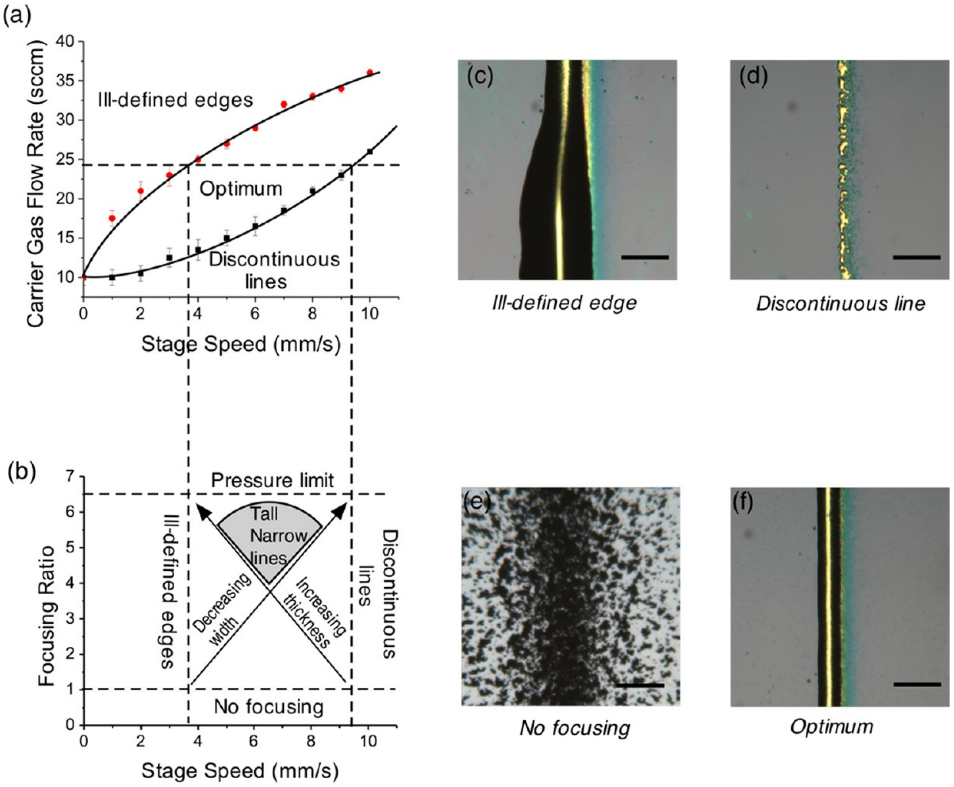

Ill-defined edge

Discontinuous line

No focusing

Optimum

Figure 12. Operability window and process regime. (a) Upper and lower bounds on the carrier gas flow rate for each stage speed determined at a fixed focusing ratio (FR = 3), and (b) operability window for a given carrier gas flow rate (24 sccm) with the region of tall and narrow lines highlighted. Optical microscope images showing (c) a line with an ill-defined edge printed at very low stage speed (1 mm/s), (d) a discontinuous line printed at very high stage speed (40 mm/s), (e) an incoherent line printed at focusing ratio less than 1, and (f) a line printed under optimized conditions. Each bar is 50 μm.

4.3. Effect of Process Parameters on Electrical Properties. The factors influencing the line geometry as discussed above also have a direct bearing on the electrical properties. The current carrying ability of a line is directly proportional to its cross-sectional area. Keeping the carrier gas flow rate and stage speed constant, the line width decreases and the thickness increases as the focusing ratio increases. To validate this argument, we measured the resistance per length for lines printed at a fixed carrier gas flow rate and stage speed for different focusing ratios. No change in resistance is seen for the same carrier gas flow rate, as shown in Figure 8a. The resistance decreases with increasing the carrier gas flow rates due to an increase in the cross-sectional area. At low carrier gas flow rates with comparable sheath gas flow rates, there is not enough solvent in the as printed feature for complete coalescence. Therefore, for the carrier gas flow rate of 14 sccm at focusing ratio 1 and 2, the deposit has low density and higher resistivity, leading to higher resistance per unit length. Increasing the focusing ratio above 2 results in more dense, well-formed lines having reduced resistivity that does not vary much over the remaining range. The resistance per unit length also increases with stage speed, as shown in Figure 8b, following almost a linear relationship up to 40 mm/s. The linear increase in resistance with stage speed suggests a decrease in the cross-sectional area but no change in the resistivity of the printed feature. Beyond a stage speed of 40 mm/s, there is inadequate coalescence of the ink upon printing and consequently the microstructure of the line becomes

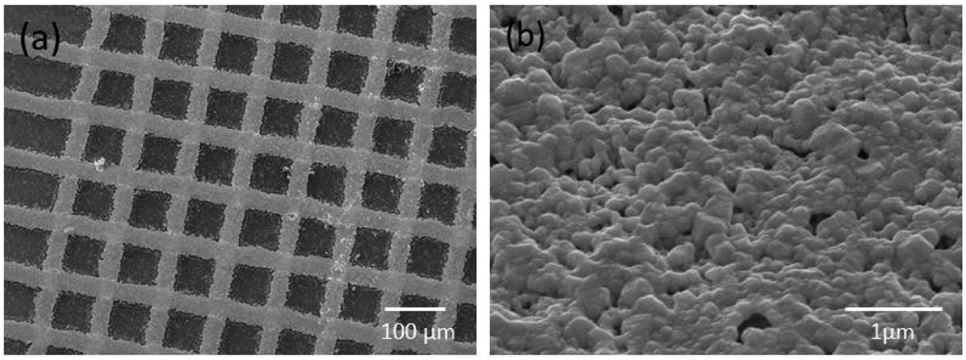

Figure 13. Characterization of sintered silver lines printed using optimized conditions. SEM micrographs showing (a) a grid of silver lines, 20 μm wide printed at carrier gas flow rate = 24 sccm, FR = 6, and stage speed = 5 mm/s; and (b) surface topography revealing sintered silver nanoparticles.

increasingly porous. Even though the lines are conductive, the resistivity is higher because of increased porosity and hence the resistance is higher than predicted by the linear relationship in Figure 8b.

4.4. Operability Window and Process Regime. Figure 12 shows an operability window with varying carrier gas flow rate and stage speed, and the impact of the focusing ratio on line geometry for a given carrier gas flow rate. As shown in Figure 12a, there is a range of stage speeds that can be selected for any given carrier gas flow rate. The limits in Figure 12a were determined experimentally with error bars representing the variability in assigning the characteristic region and lines drawn to represent the boundaries. At low stage speeds, the input from the impinging aerosol jet cannot be accommodated in the printed line, but rather forms an irregular, ill-defined deposit. On the other hand, above a critical stage speed there is insufficient material in the impinging aerosol jet and the printed line becomes discontinuous. Figure 12a was gathered for a single focusing ratio, but the bounds shown were not very sensitive to the focusing ratio and so the process window can be applied over a range of printing conditions. Focusing ratio does, however, have a dramatic impact on the line characteristics.

Figure 12b shows the effect of the focusing ratio and the stage speed at a constant carrier gas flow rate. The figure shows an example with a carrier gas flow rate of 24 sccm; the bounds on stage speeds from Figure 12a are translated to Figure 12b. The upper bound of the focusing ratio for the stated carrier gas flow rate is 6.5, limited by the maximum allowable pressure of the gases inside the nozzle. The lower bound is at FR =1 , below which there are no coherent lines. The four bounds create an operability window. This process could be repeated for each of the carrier gas flow rates. The role of the focusing ratio is shown in the window. Higher focusing ratios are a key to getting both low line widths and high thicknesses. Too slow a stage speed increases the line width. However, too high a stage speed reduces both the line width and thickness. Therefore, each operability window has a domain for low line widths and high aspect ratio lines. Referring again to Figure 12a, it is important to note that increasing the carrier gas flow rate has the effect of shifting the operability window to higher deposition speeds. However, the upper bound of focusing ratio (Figure 12b) is also brought down simultaneously, thereby shrinking the operability window. Also, the operability window may require additional limits based on studies of the correlation between overspray and process variables.

A demonstration of lines printed in the "tall and narrow" regime of the operability window is shown in Figure 13. A grid of silver lines, 20 μm wide and about 2 μm tall, was printed in a single pass at a carrier gas flow rate of 24 sccm, focusing ratio of 6, and stage speed of 5 mm/s using a 200 μm nozzle.

5. CONCLUSIONS

A systematic study of aerosol jet printing process variables revealed conditions for creating tall and narrow conductive silver lines in a single pass, and a simple model based on continuity between the aerosol beam and the printed line was used to explain the impact of these adjustable parameters on the printed line geometry. The concept of focusing ratio, the ratio of the sheath gas flow rate to the carrier gas flow rate, was introduced and shown to be central to the printing process. The focusing ratio alone determines the line width so long as postdeposition spreading is minimal. Narrower lines are created at high focusing ratios. Line thickness was found to increase with focusing ratio and carrier gas flow rate, but decrease with stage speed. The decrease in thickness and hence the increase in the line resistance with increasing stage speed could be offset by increasing the carrier gas flow rate at fixed focusing ratio. To define printing conditions and optimize them for electrical function, an operability window was defined and the regime for tall and narrow lines identified. Under the optimized conditions, lines as narrow as 20 μm with an aspect ratio of 0.1 were printed in a single pass.

■ ASSOCIATED CONTENT

Ⓢ Supporting Information

Additional figures and description (PDF). This material is available free of charge via the Internet at http://pubs.acs.org.

■ AUTHOR INFORMATION

Corresponding Author

*E-mail: lfrancis@umn.edu; frisbie@umn.edu.

Notes

The authors declare no competing financial interest.

■ ACKNOWLEDGMENTS

The authors thank the Office of Naval Research for financial support through the Multi-University Research Initiative (MURI Award N00014-11-1-0690). We thank Yuri Didenko of UT Dots, Inc. We owe our gratitude to Kyle Price, Yanfei Wu, Kihyon Hong, Se Hyun Kim, and Wieslaw Suszynski for their contributions to this project. Parts of this work were carried out at the Characterization Facility and the Nanofabrication Center of the University of Minnesota.

REFERENCES

(1) Howard, W. E. *Sci. Am.* **2004**, February, 76−81.

(2) Liang, T. X.; Sun, W. Z; Wang, L. D.; Wang, Y. H; Li, H. D. *IEEE Trans. Components, Packag. Manuf. Technol., Part B* **1996**, *19*, 423−426.

(3) Soltman, D.; Subramanian, V. *Langmuir* **2008**, *24*, 2224−2231.

(4) Schmidt, G. C.; Bellmann, M.; Meier, B.; Hambsch, M.; Reuter, K.; Kempa, H.; Hübler, A. C. *Org. Electron.* **2010**, *11*, 1683−1687.

(5) Noh, J.; Yeom, D.; Lim, C.; Cha, H.; Han, J.; Kim, J.; Park, Y.; Subramanian, V.; Cho, G. *IEEE Trans. Electron. Packag. Manuf.* **2010**, *33*, 275−283.

(6) Kopola, P.; Zimmermann, B.; Filipovic, A.; Schleiermacher, H.; Greulich, J.; Rousu, S.; Hast, J.; Myllyla, R.; Wurfel, U. *Sol. Energy Mater. Sol. Cell.* **2012**, *107*, 252−258.

(7) Liu, R.; Ding, H.; Lin, J.; Shen, F.; Cui, Z.; Zhang, T. *Nanotechnology* **2012**, *23*, 505301.

(8) Goth, C.; Putzo, S.; Franke, J. *IEEE 61st Electronic Components and Technology Conference (ECTC)*; Lake Buena Vista, FL, May 31−June 3, 2011 ; IEEE: Piscataway, NJ, 2011; pp 1211−1216.

(9) Renn, M. J. U.S. Patent 7108894 B2, 2006.

(10) Braga, D.; Erickson, N.; Renn, M. J.; Holmes, R. J.; Frisbie, C. D. *Adv. Funct. Mater.* **2012**, *22*, 1623−1631.

(11) Cho, J. H.; Lee, J.; Xia, Y.; Kim, B.; He, Y.; Renn, M. J.; Lodge, T. P.; Frisbie, C. D. *Nat. Mater.* **2008**, *7*, 900−906.

(12) Xia, Y.; Zhang, W.; Ha, M.; Cho, J. H.; Renn, M. J.; Kim, C. H.; Frisbie, C. D. *Adv. Funct. Mater.* **2010**, *20*, 587−594.

(13) Jones, C. S.; Lu, X.; Renn, M.; Stroder, M.; Shih, W. *Microelectron. Eng.* **2010**, *87*, 434−437.

(14) Zhao, J.; Gao, Y.; Lin, J.; Chen, Z.; Cui, Z. *J. Mater. Chem.* **2012**, *22*, 2051−2056.

(15) Maiwald, M.; Werner, C.; Zoellmer, V.; Busse, M. *Sens. Actuators, A* **2009**, *1*, 907−910.

(16) Joo, S.; Baldwin, D. F. *IEEE Trans. Electron. Packag. Manuf.* **2010**, *33*, 129−134.

(17) Lesch, A.; Momotenko, D.; Cortes-Salazar, F.; Wirth, I.; Tefashe, U. M.; Meiners, F.; Vaske, B.; Girault, H. H.; Wittstock, G. *J. Electroanal. Chem.* **2012**, *666*, 52−61.

(18) Sukeshini, A. M.; Jenkins, T.; Gardner, P.; Miller, R. M.; Reitz, T. L. *ASME 8th International Conference on Fuel Cell Science, Engineering and Technology*; American Society of Mechanical Engineers: New York, 2010; Vol. *1*, pp 325−332.

(19) Sukeshini, A. M.; Gardner, P.; Meisenkothen, F.; Jenkins, T.; Miller, R.; Rottmayer, M.; Reitz, T. L. *ECS Trans.* **2011**, *35*, 2151−2160.

(20) Mette, A.; Richter, P. L.; Horteis, M.; Glunz, S. W. *Prog. Photovolt.* **2007**, *15*, 621−627.

(21) Yang, C.; Zhou, E.; Miyanishi, S.; Hashimoto, K.; Tajima, K. *ACS Appl. Mater. Interfaces* **2011**, *3*, 4053−4058.

(22) Horteis, M.; Glunz, S. W. *Prog. Photovolt.* **2008**, *16*, 555−560.

(23) Kalio, A.; Richter, A.; Hörteis, M.; Glunz, S. W. *Energy Procedia* **2011**, *8*, 571−576.

(24) Kalio, A.; Leibinger, M.; Filipovic, A.; Kruger, K.; Glatthaar, M.; Wilde, J. *Sol. Energy Mater. Sol. Cell.* **2012**, *106*, 51−54.

(25) Verheecke, W.; Van Dyck, M.; Vogeler, F.; Voet, A.; Valkenaers, H. *8th International DAAAM Baltic Conference "Industrial Engineering"*; Tallinn, Estonia, April 19−21, 2012 ; Danube Adria Association for Automation & Manufacturing: Vienna, Austria, 2012; pp 373-379.

(26) Dearden, A. L.; Smith, P. J.; Shin, D. Y.; Reis, N.; Derby, B.; O'Brien, P. *Macromol. Rapid Commun.* **2005**, *26*, 315−318.

(27) Russo, A.; Ahn, B. Y.; Adams, J. J.; Duoss, E. B.; Bernhard, J. T.; Lewis, J. A. *Adv. Mater.* **2011**, *23*, 3426−3430.